Supporting information

Multifunctional zeolite film enables stable high-voltage operation of LiCoO₂ cathode

Zezhou Lin[1,2#], Yiran Ying[1#], Zhihang Xu[1], Gao Chen[1], Xi Gong[1], Zehua Wang[2], Daqin Guan[2], Leqi Zhao[2], Mingyang Yang[3], Ke Fan[1], Tiancheng Liu[1], Hao Li[1], Honglei Zhang[1], Huangxu Li[1], Xi Zhang[4], Ye Zhu[1], Zhouguang Lu[3], Zongping Shao[2*], Peiyu Hou[5*] and Haitao Huang[1*]

[1] Department of Applied Physics, The Hong Kong Polytechnic University, Hong Kong 999077, China;

[2] WA School of Mines: Minerals, Energy and Chemical Engineering, Curtin University, Bently, WA 6102, Australia;

[3] Department of Materials Science and Engineering, Shenzhen Key Laboratory of Interfacial Science and Engineering of Materials, Southern University of Science and Technology, Shenzhen 518055, China;

[4] Institute of Nanosurface Science and Engineering, Guangdong Provincial Key Laboratory of Micro/Nano Optomechatronics Engineering, Shenzhen University, Shenzhen 518060, China;

[5] School of Physics and Technology, University of Jinan, Jinan, Shandong 250022, China;

Experimental Section

Material

The purchased lithium cobalt oxide (LiCoO$_2$, 98%, International laboratory USA), Pseudo-bohemite (AlOOH), Phosphoric acid (H$_3$PO$_4$, 85%, International laboratory USA), and Triethylamine (TEA, 99%, International laboratory USA) were directly used without purification.

Material synthesis

LCO@A and LCO@Z were prepared by hydrothermal method. For LCO@A, pristine LCO was mixed with pseudo-bohemite and phosphoric acid in deionized water. For LCO@Z, pristine LCO was mixed with pseudo-bohemite, phosphoric acid, and triethylamine in deionized water. Both LCO@A and LCO@Z were processed under hydrothermal condition at 155°C for 1 h and the collected powders were annealed at 550°C for 2 h.

Materials Characterization

The morphology and phase of cathodes were investigated by scanning electron microscope (SEM, MAIA3) and X-ray diffraction (XRD, Rigaku SmartLab). Cross-sectional samples were prepared by an ion Milling System (IM4000plus) and the cross-sectional images were observed using FE-SEM (Regulus8100). The microstructure of LCO@Z was studied by Transmission Electron Microscope (TEM, JEOL JEM-2100F). The Co-L_3-edge X-ray absorption spectroscopy (XAS) data of cathodes were collected at the TLS 16A beamline, NSRRC, Taiwan. The chemical composition of the cycled cathode was investigated using a time-of-flight secondary ion mass spectroscopy (TOF-SIMS) equipment (IONTOF M6,

Germany). A dual beam depth profiling method was used, combining a 30 keV Bi^{++} primary ion source that delivered 0.2 pA of target current over an area of 100×100 μm^2 for analysis, with a 1 keV Cs^+ sputter beam that delivered ≈ 90 nA of target current over an area of 300×300 μm^2 to create a sputtered crater. The surface components analysis was studied by X-Ray Photoelectron Spectroscopy (XPS, Thermo Fisher Scientific Nexsa). The specific surface area of powders was determined by Brunauer, Emmett, and Teller method (BET, ASAP 2020). *In-situ* XRD patterns were obtained using a specially designed cell with a beryllium (Be) window and at a scan range from 10° to 80°, scan rate = 10° min^{-1}. Elemental ratios in the samples were determined using inductively coupled plasma optical emission spectroscopy (ICP-OES, Agilent 7700). Electrode conductivity of electrodes was conducted using automatic four-point probe powder resistivity instrument (ST2742B).

Electrochemical Measurement

To fabricate the electrodes, a slurry was prepared by dissolving 90% active material particles (LCO, LCO@A, and LCO@Z), 5 wt% super P, and 5 wt% polyvinylidene fluoride (PVdF) in an appropriate amount of N-methyl-1,2-pyrrolidone (NMP). The mass loading of active oxide in the slurry was set to ~4 and >10 mg cm^{-2} in half cells. The electrodes were prepared by punching the slurry onto a substrate with a diameter of 12 mm under a compression pressure of 2 MPa. In coin-type half cells, lithium metal was used as the anode. The electrolyte used in the half cells consisted of 1 M $LiPF_6$ dissolved in a mixture of ethylene carbonate (EC) and dimethyl carbonate (DMC) in a volume ratio of 1:1. The electrochemical tests were conducted at room temperature (25°C) and high temperature (60°C) using a LAND instrument (CT-2001 A). Galvanostatic intermittent titration technique (GITT) measurements were performed on

the half cells within the voltage range of 3.0-4.6 V (vs. Li/Li$^+$). A titration current of 0.3C (1C = 200 mA·g^{-1}) was applied for 10 minutes, followed by a relaxation time of 1 hour to allow the system to reach the quasi-equilibrium potential. Cyclic voltammetry (CV) and electrochemical impedance spectroscopy (EIS) were conducted using a Solartron 1470E instrument (AMETEK, USA). The frequency range for EIS measurements was 10^{-2} to 10^6 Hz. Differential Electrochemical Mass Spectrometer (DEMS, QAS100 Li) were used for detecting the gas generation during charging and discharging of the anode material in a Swagelok-type cell, and the carrier gas was Argon with a flow rate of 1 mL min^{-1}.

Computational Methods

All spin-polarized density functional theory (DFT) calculations were performed by using the projector-augmented wave method in VASP code[1, 2]. Perdew-Burke-Ernzerhof (PBE) scheme of generalized gradient approximation was applied as the exchange-correlation functional[3]. The van der Waals corrections were considered by Grimme's DFT-D3 method[4]. Kinetic energy cutoff was set as 420 eV, and K-points meshes with density higher than $0.035 \times 2\pi$ Å^{-1} were used for Brillouin zone sampling. All structures were relaxed until energy and force convergence criteria of 10^{-5} eV and 0.02 eV Å^{-1} were reached, respectively. Hubbard U correction term of 3.32 eV was applied on strongly correlated cobalt atoms[5]. The adsorption energy ΔE was calculated as $\Delta E = E_{surface-ad} - E_{surface} - E_{ad}$, where $E_{surface-ad}$, $E_{surface}$, and E_{ad} represent DFT-calculated energies of surface with adsorption, clean surface, and adsorbate, respectively. Vacuum layers with a thickness of at least 15 Å were added to the slab structures to prevent spurious interactions. The climbing-image nudged elastic band (CI-NEB) method was used for calculating the diffusion barriers[6].
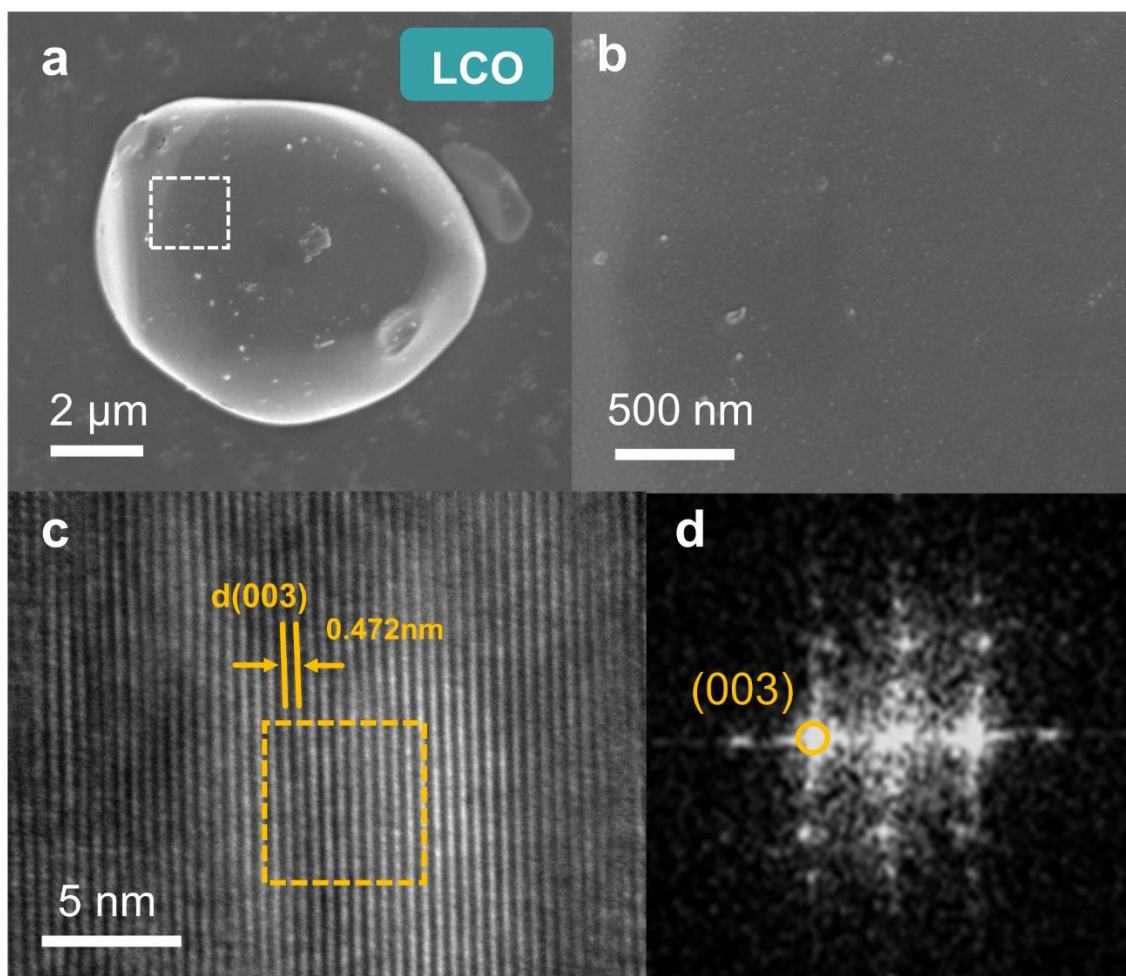
Fig. S1 a SEM image of pristine LCO, and **b** magnified area of the white rectangle in **a**. **c** HRTEM image of pristine LCO and **d** FFT pattern of the orange rectangle in **c**.
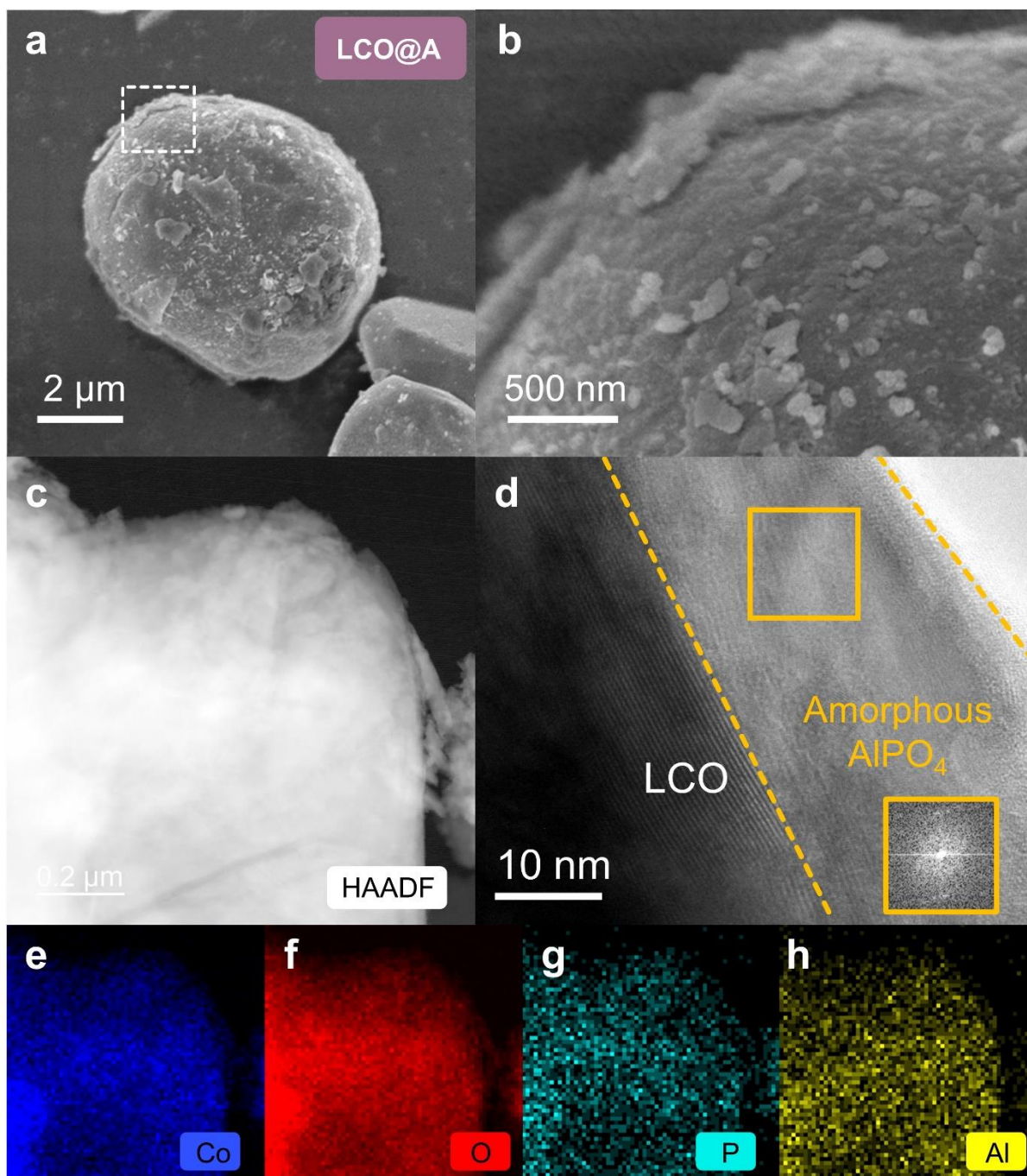
Fig. S2 a SEM image of LCO@A, and **b** magnified area of the white rectangle in **a**. **c** HAADF and **d** HRTEM images of LCO@A and elemental distribution of **e** Co, **f** O, **g** P and **h** Al.
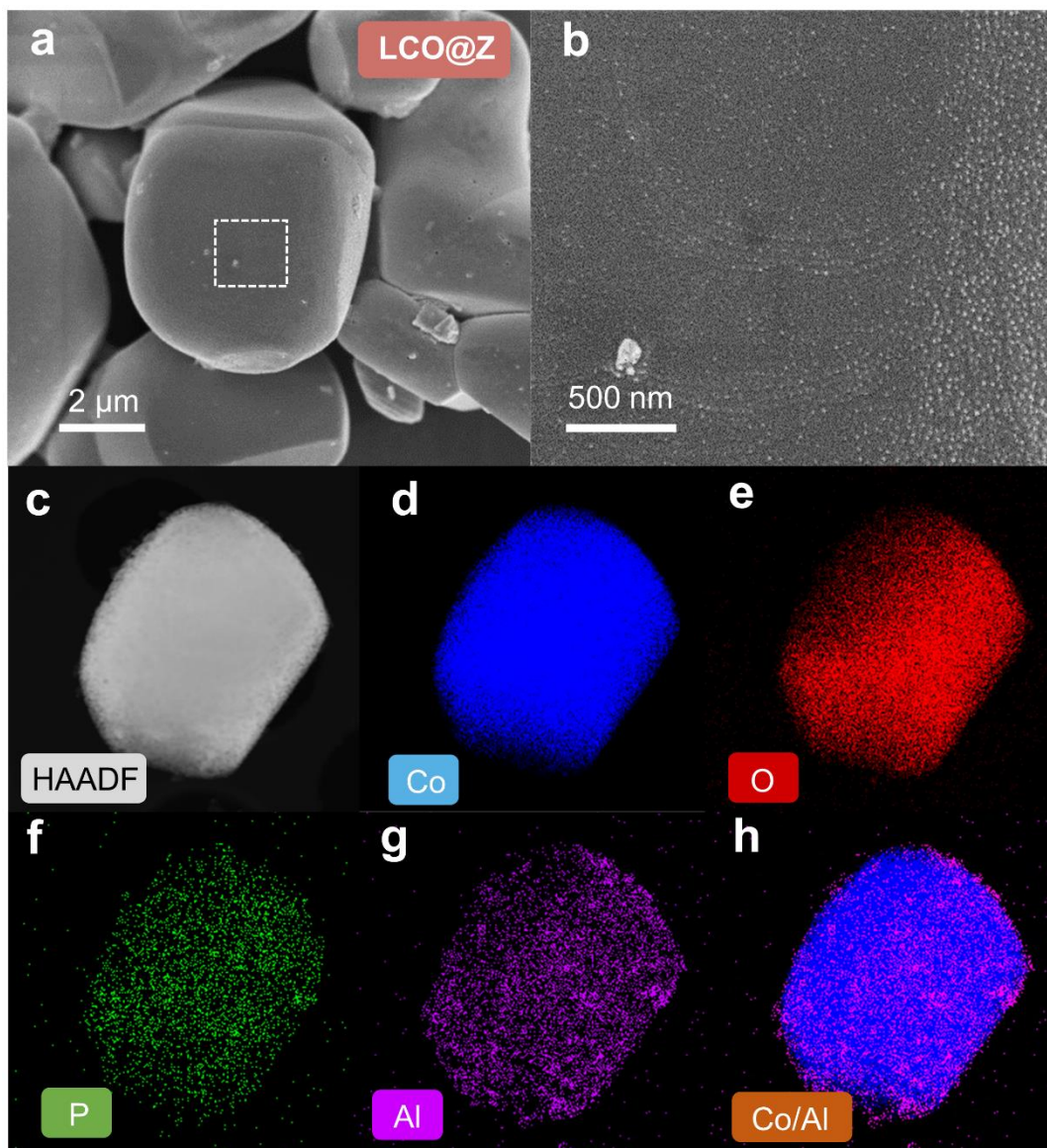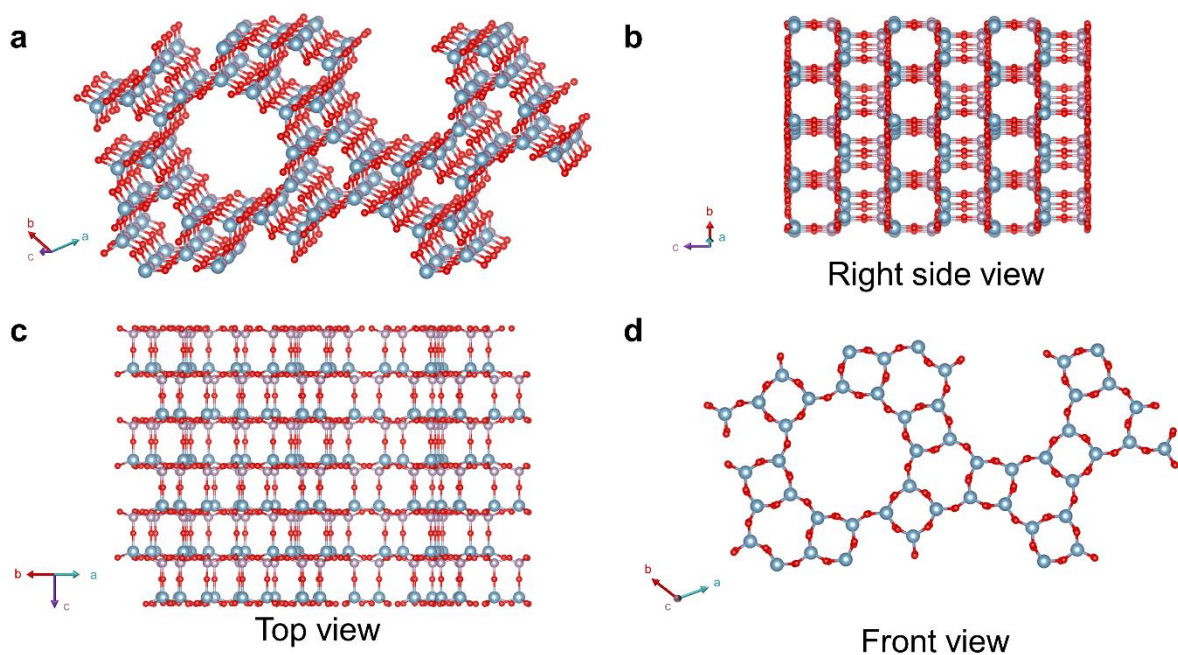
Fig. S3 a SEM image of LCO@Z, and **b** magnified area of the white rectangle in **a**. **c** HAADF image of LCO@Z and elemental distribution of **d** Co, **e** O, **f** P, **g** Al and **h** Co/Al mixed.

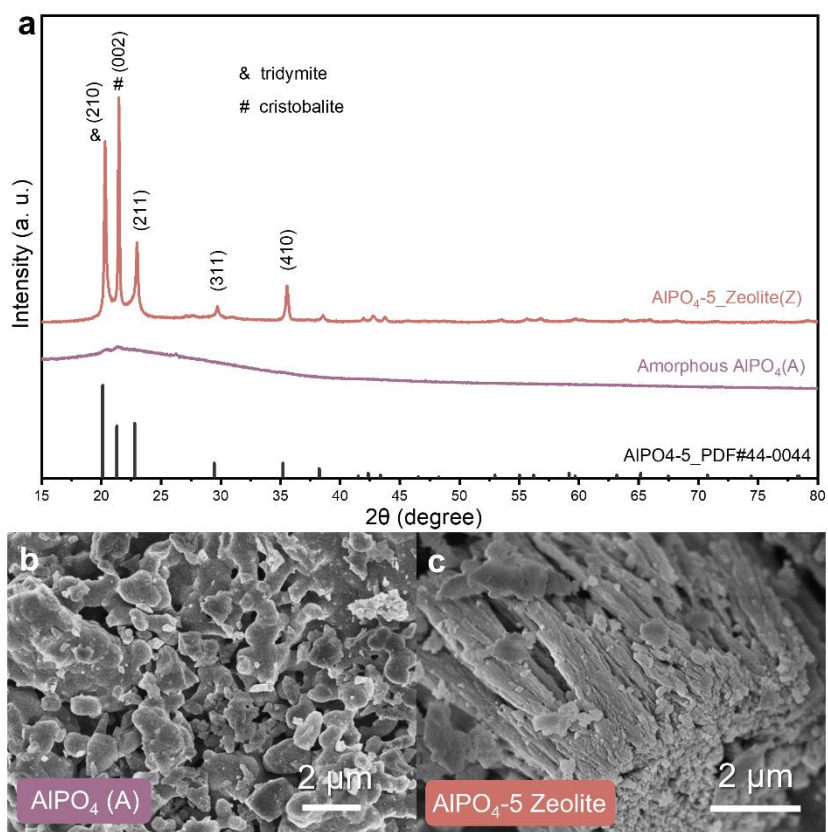**Fig. S4** Three view of the atomic structure of the (210) slab of AlPO$_4$-5 zeolite.

Fig. S5 a XRD patterns of AlPO$_4$-5 zeolite and amorphous AlPO$_4$. SEM image of **b** amorphous AlPO$_4$ and **c** AlPO$_4$-5 zeolite.
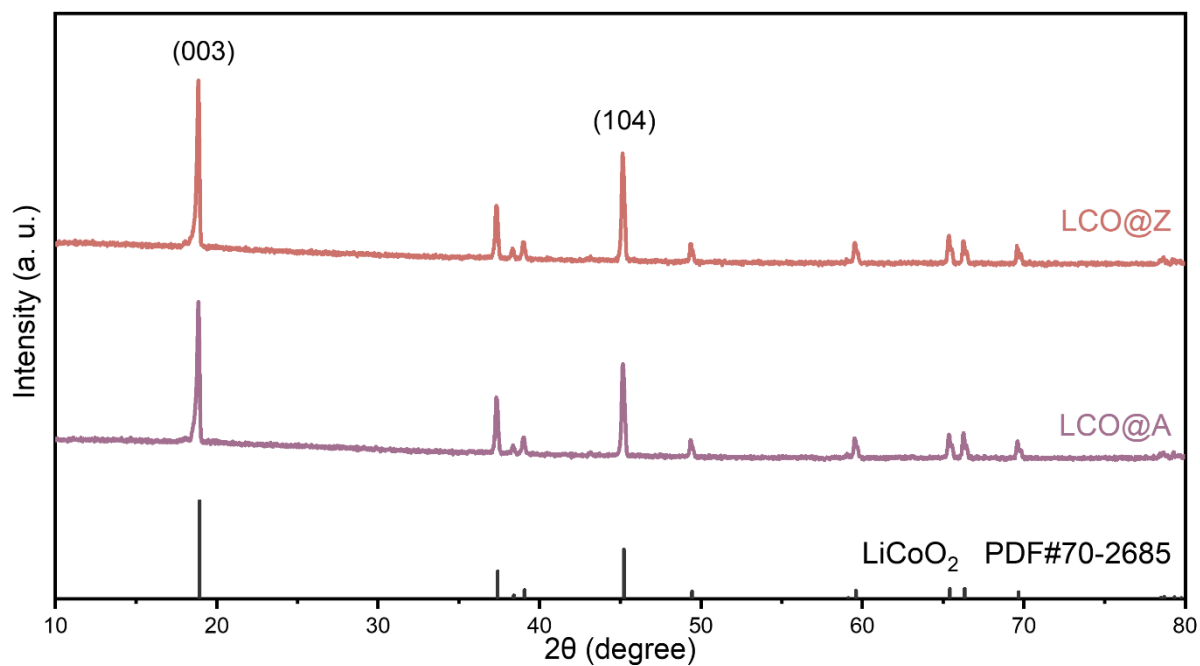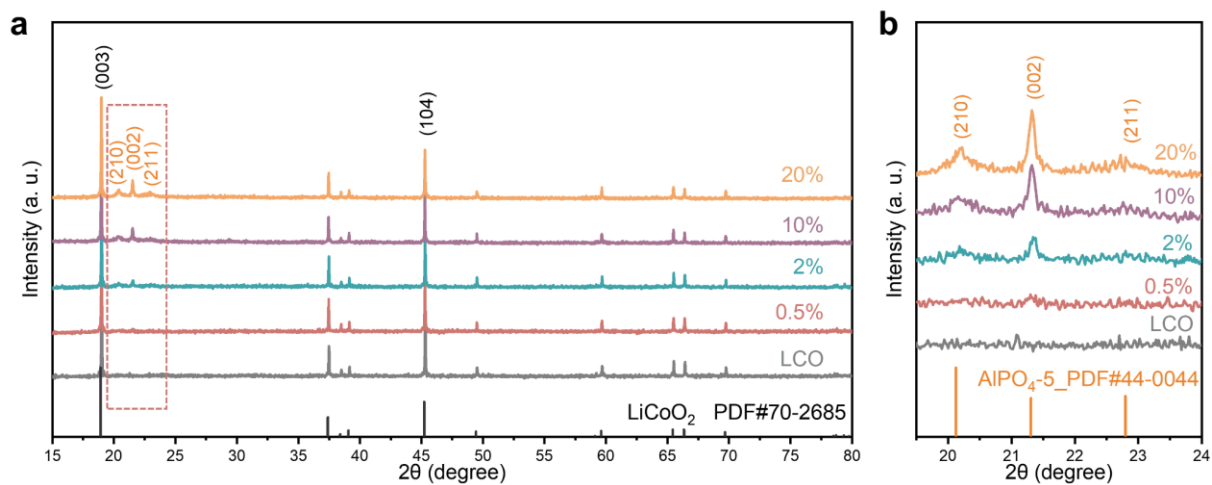
Fig. S6 XRD patterns of as-prepared LCO@A and LCO@Z samples.

Fig. S7 XRD patterns of LCO and LCO@Z samples, with the concentration of the precursor of AlPO$_4$-5 in LCO@Z varying from 0.5% to 20%.
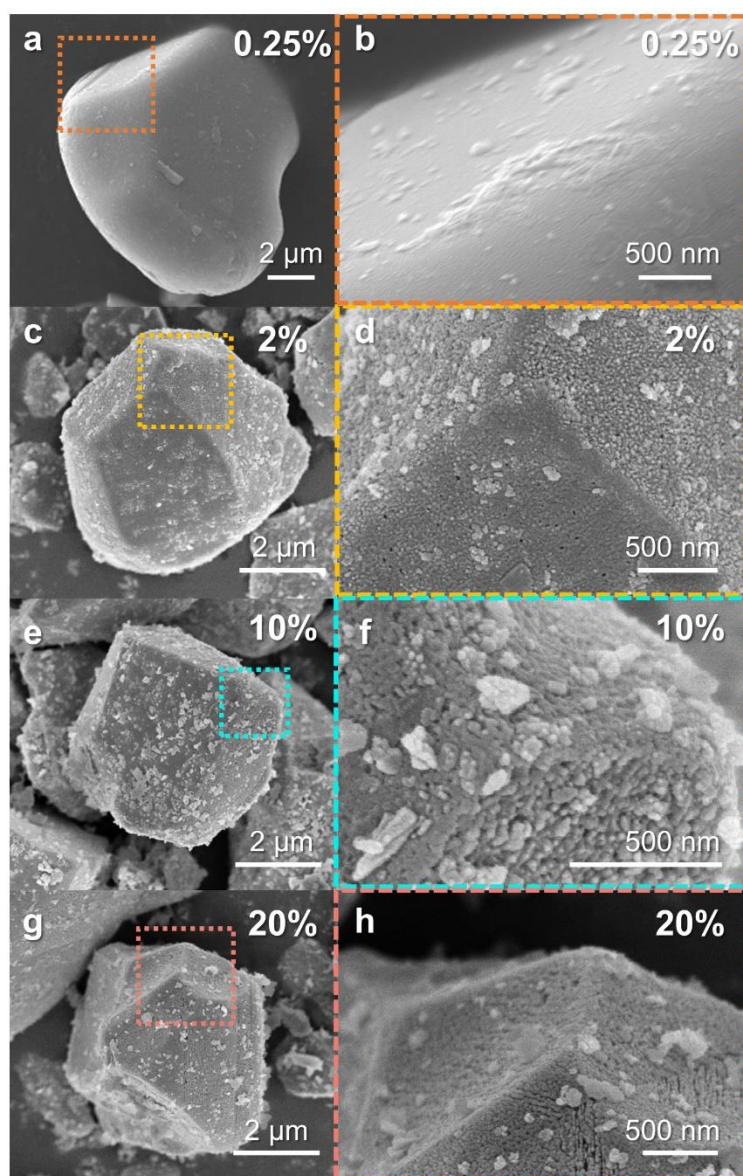
Fig. S8 SEM images of LCO@Z samples. The concentration of AlPO$_4$-5 precursor varies from 0.25% to 20%.
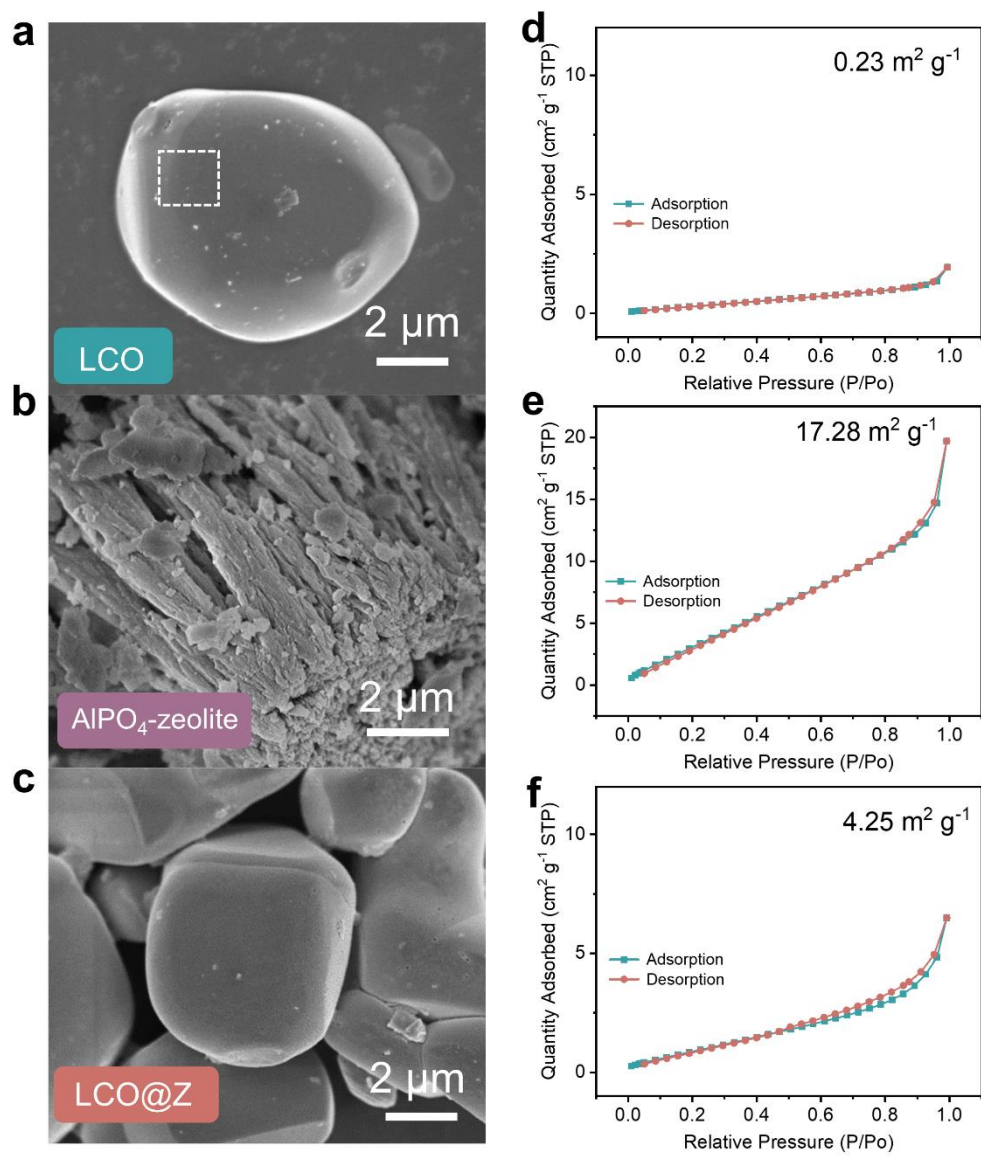
Fig. S9 SEM images of **a** LCO, **b** AlPO₄-5 zeolite and **c** LCO@Z. The corresponding

Brunauer-Emmett-Teller (BET) result of **d** LCO, **e** AlPO₄-5 zeolite and **f** LCO@Z.
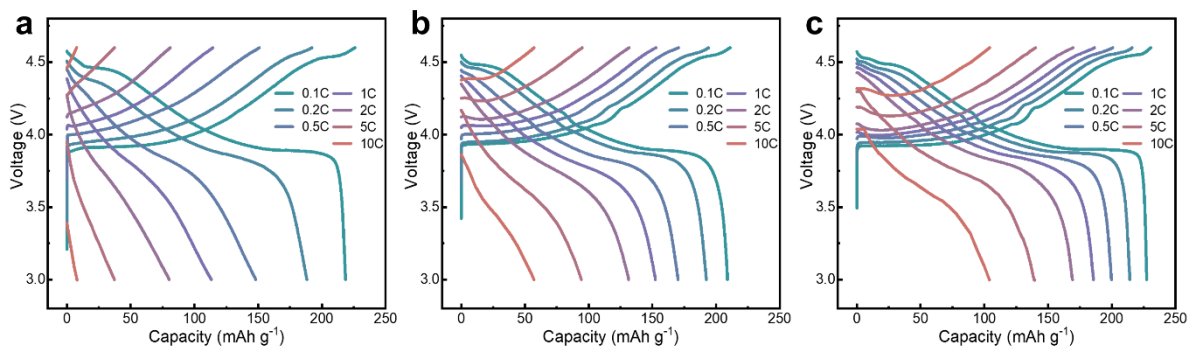
Fig. S10 Continuous charge/discharge curves under an upper cut-off voltage of 4.6 V (vs. Li/Li$^+$) from 0.1C to 10C of **a** LCO, **b** LCO@A and **c** LCO@Z.
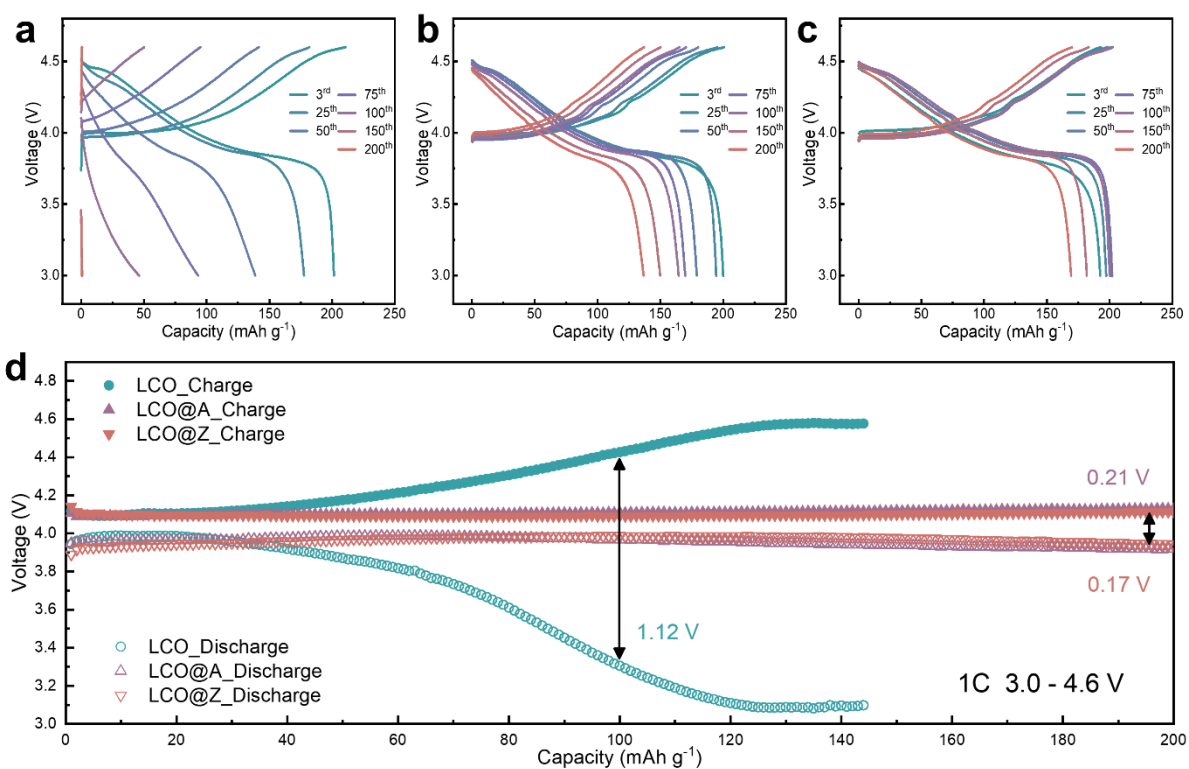

Fig. S11 Continuous charge/discharge curves from 3rd to 200th cycles of **a** LCO, **b** LCO@A and **c** LCO@Z at 1C under an upper voltage of 4.6 V (vs. Li/Li$^+$). **d** Cycling performance of mid-point voltage of LCO, LCO@A, and LCO@Z at 1C under an upper voltage of 4.6 V (vs. Li/Li$^+$).
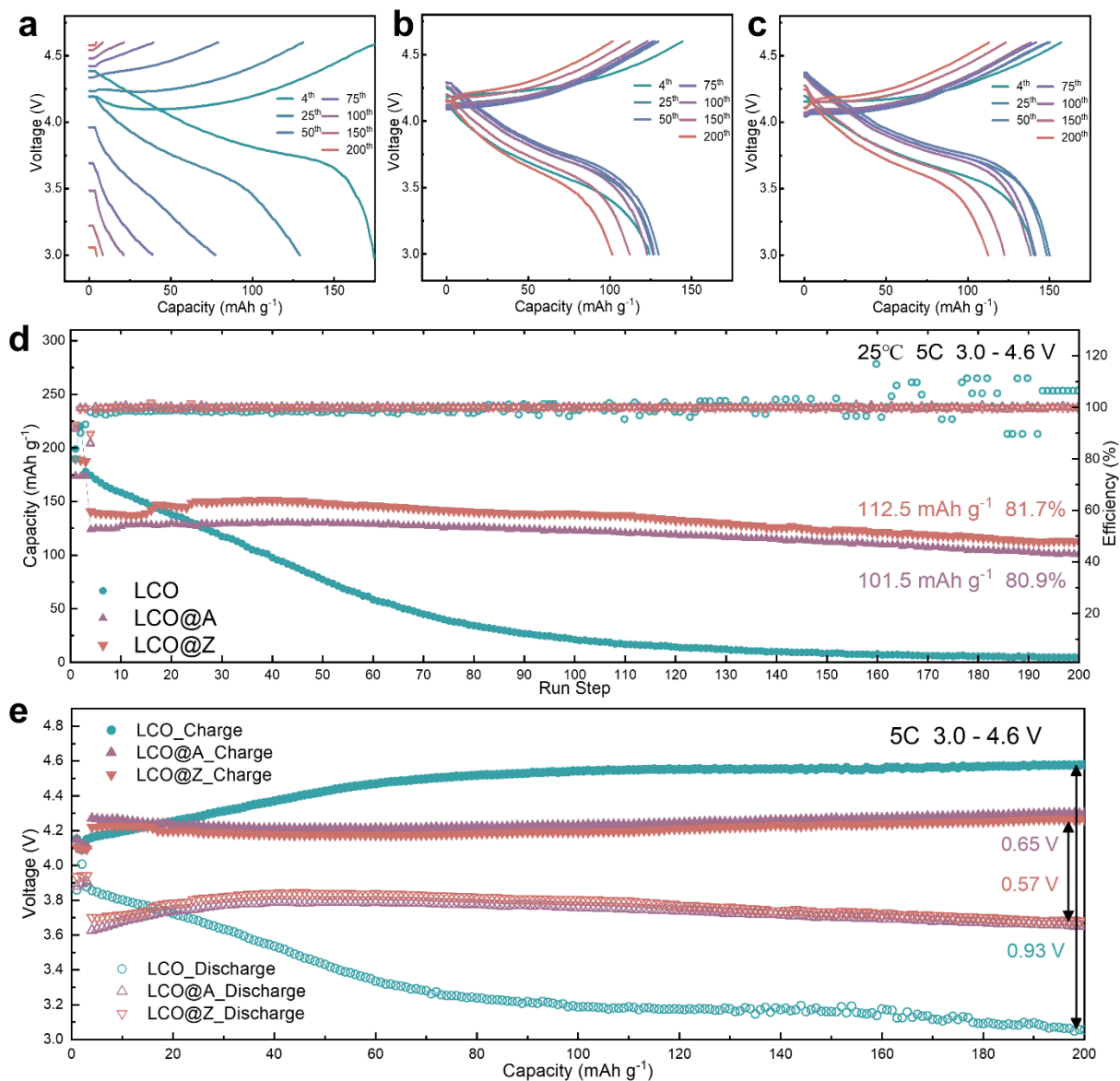
Fig. S12 High rate (5C) electrochemical performance. Continuous charge/discharge curves from the 4th to the 200th cycles of **a** LCO, **b** LCO@A and **c** LCO@Z at 5C under an upper cut-off voltage of 4.6 V (vs. Li/Li$^+$). **d** Cycling stability of half-cell at 5C under an upper cut-off voltage of 4.6 V (vs. Li/Li$^+$) from 1st to 200th cycles. **e** Cycling performance of mid-point voltages of LCO, LCO@A, and LCO@Z at 5C under an upper cut-off voltage of 4.6 V (vs. Li/Li$^+$).

Fig. S13 High temperature (60°C) electrochemical performance. Continuous charge/discharge curves from the 3rd to the 100th cycles of **a** LCO, **b** LCO@A and **c** LCO@Z at 1C under an upper cut-off voltage of 4.6 V (vs. Li/Li$^+$). **d** Cycling stability of half-cell at 1C under an upper cut-off voltage of 4.6 V (vs. Li/Li$^+$) from 1st to 100th cycles. **e** Cycling performance of mid-point voltages of LCO, LCO@A, and LCO@Z at 1C under an upper cut-off voltage of 4.6 V (vs. Li/Li$^+$).
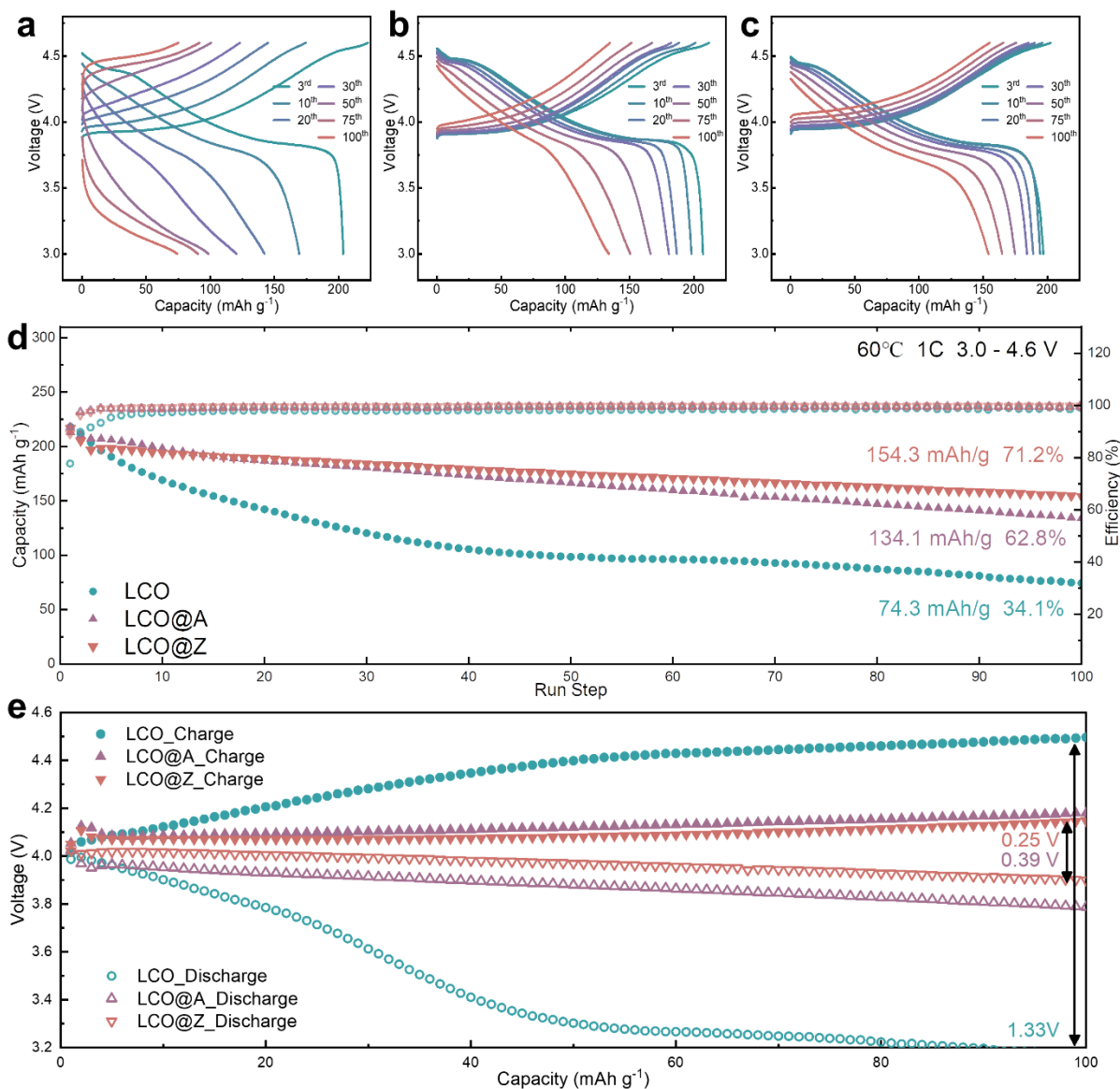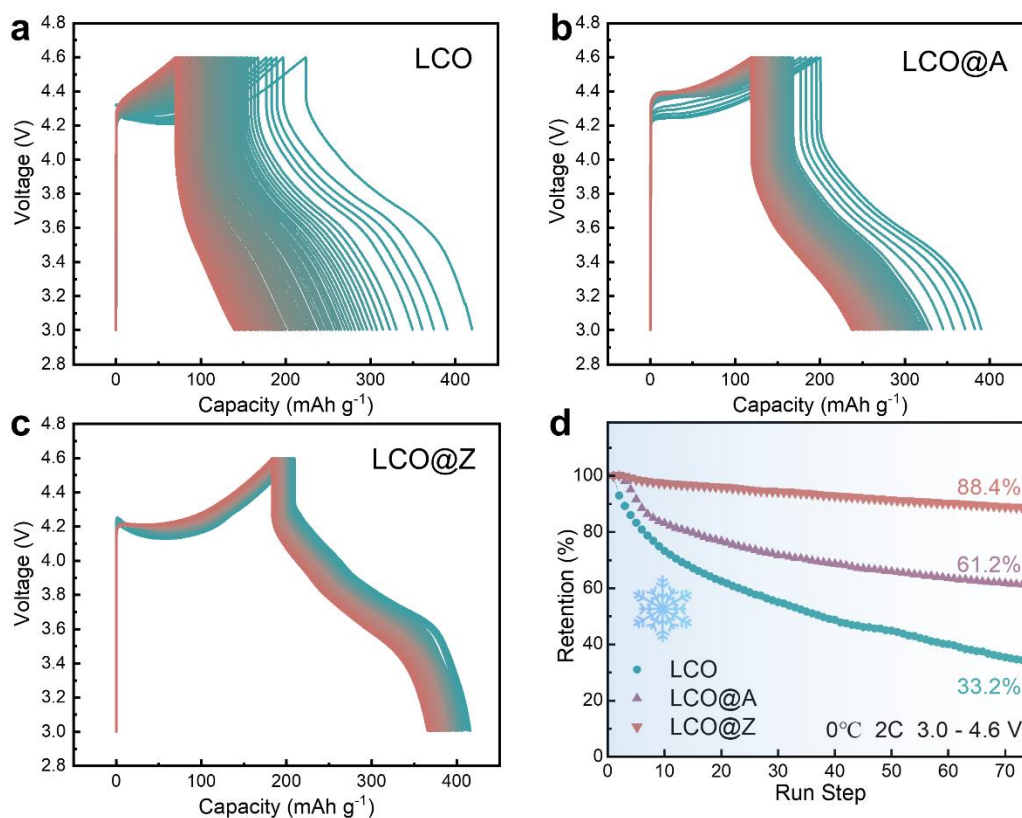
Fig. S14 Low temperature (0°C) electrochemical performance. Continuous charge/discharge curves from the 1st to the 75th cycles of **a** LCO, **b** LCO@A and **c** LCO@Z at 2C under an upper cut-off voltage of 4.6 V (vs. Li/Li$^+$). **d** Cycling stability of half-cells at 2C under an upper cut-off voltage of 4.6 V (vs. Li/Li$^+$) from 1st to 75th cycles at 0°C.
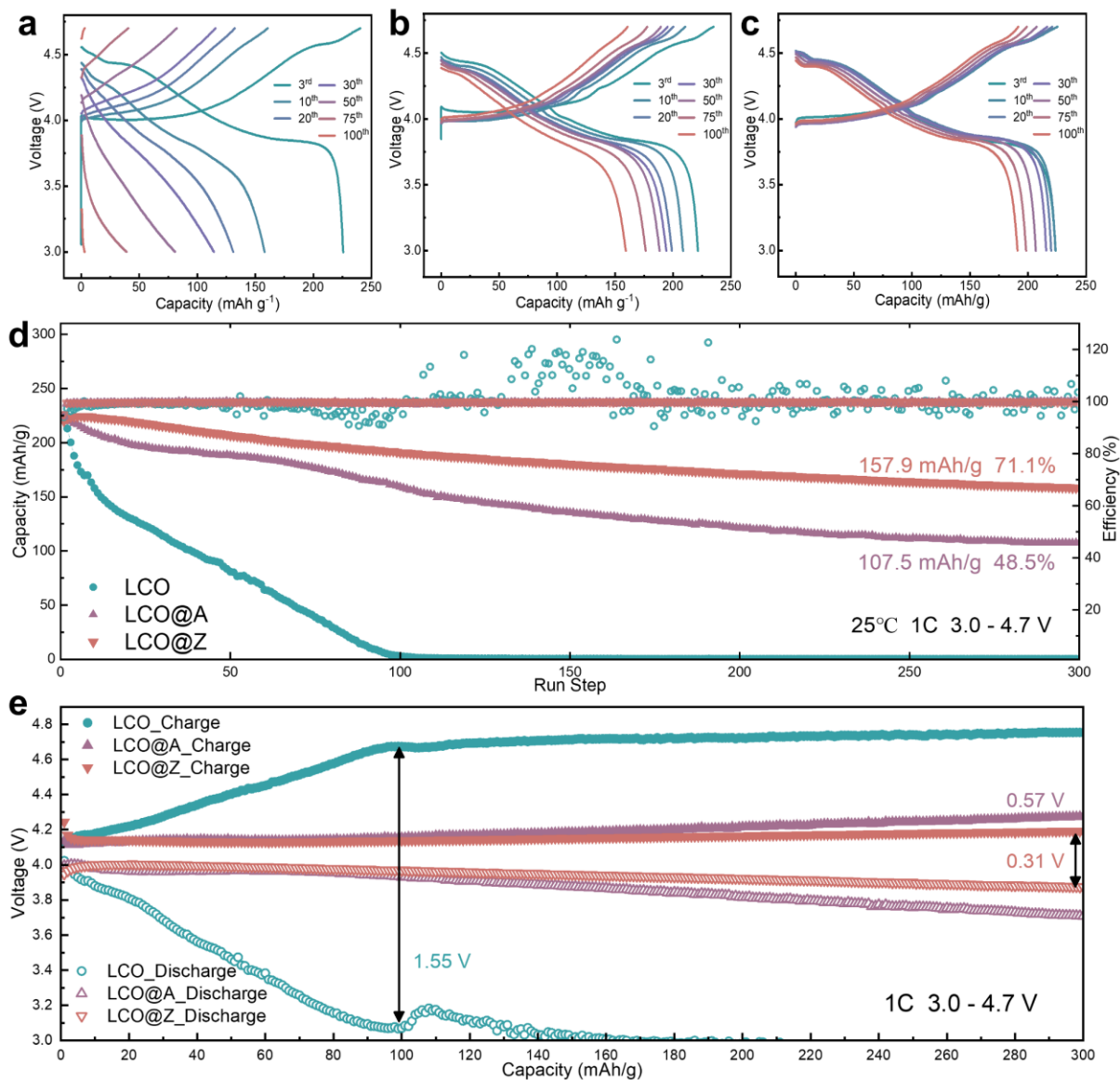
Fig. S15 High voltage (4.7 V vs. Li/Li$^+$) electrochemical performance. Continuous charge/discharge curves from the 3rd to the 100th cycles of **a** LCO, **b** LCO@A and **c** LCO@Z at 1C under an upper cut-off voltage of 4.7 V. **d** Cycling stability of half-cell at 1C under an upper cut-off voltage of 4.7 V from 1st to 300th cycles. **e** Cycling performance of mid-point voltages of LCO, LCO@A, and LCO@Z at 1C under an upper cut-off voltage of 4.7 V.
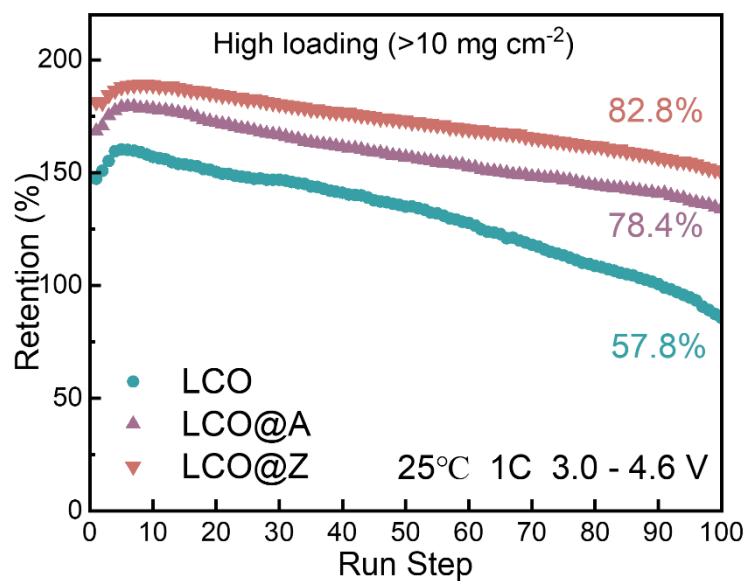
Fig. S16 Cycling performance of high mass loading (> 10 mg cm^{-2}) cathode of LCO, LCO@A and LCO@Z at 1C under an upper cut-off voltage of 4.6 V (vs. Li/Li$^+$).
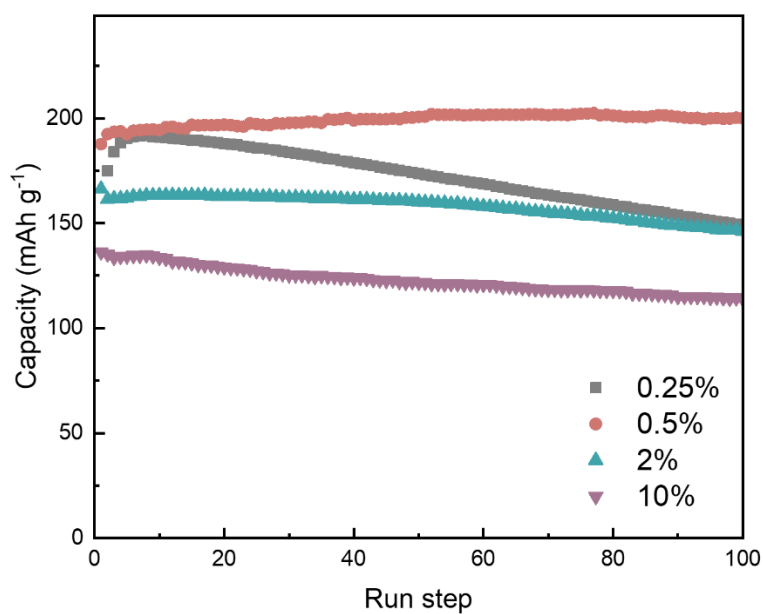
Fig. S17 Cycling stability of LCO@Z samples (with the concentration of AlPO$_4$-5 precursor increasing from 0.25% to 10%) at 1C under an upper cut-off voltage of 4.6 V from 1st to 100th cycles.
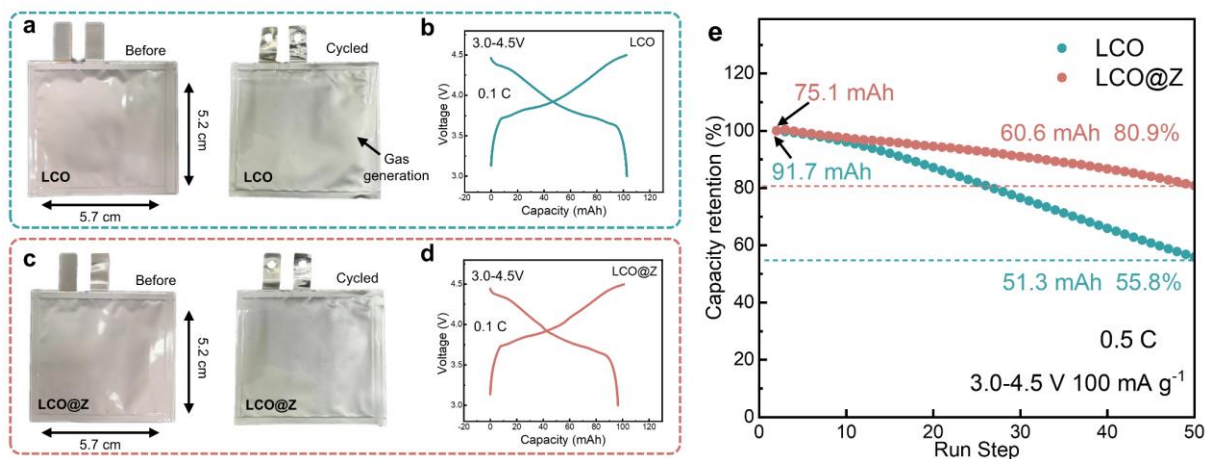
Fig. S18 LCO∥graphite pouch cell. Photo of the assembled pouch cell of **a** LCO and **c** LCO@Z before and after cycling. The first cycle of **b** LCO and **d** LCO@Z at 0.1C. **e** Cycling stability of pouch cells of LCO and LCO@Z at 3.0-4.5 V (vs. graphite).
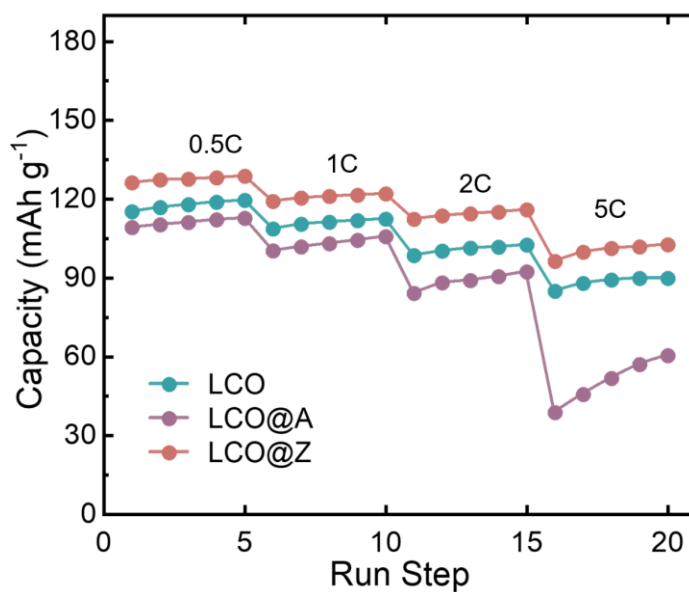
Fig. S19 Rate capability of LCO, LCO@A and LCO@Z at 3.0-4.2 V from 0.5C to 10C.
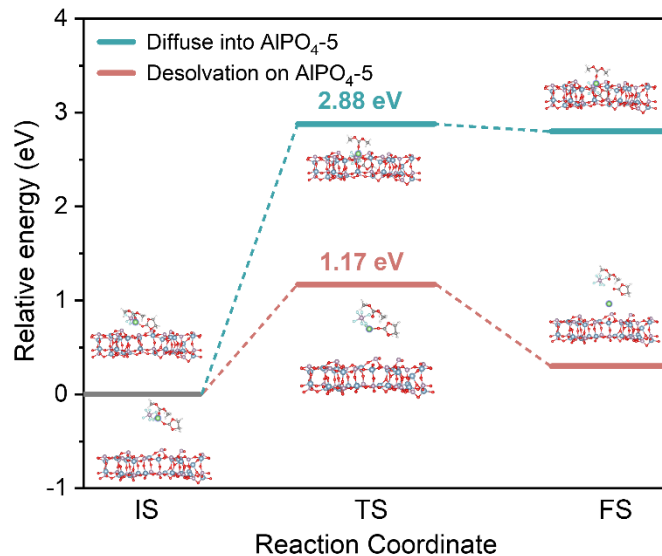
Fig. S20 DFT-calculated energy barriers (in eV) for the diffusion of Li-EC-DMC-PF$_6$ complex into the 10.2 Å-pore of AlPO$_4$-5 and Li$^+$-desolvation on AlPO$_4$-5.
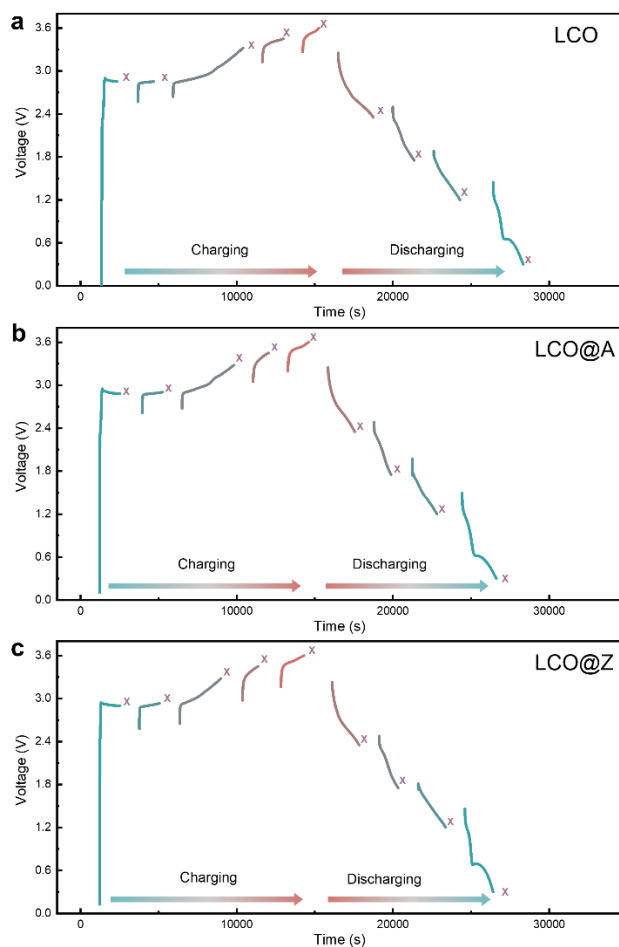
Fig. S21 The charging and discharging curves of **a** LCO, **b** LCO@A, and **c** LCO@Z electrodes in the second cycle during *in-situ* EIS measurements.

LCO:
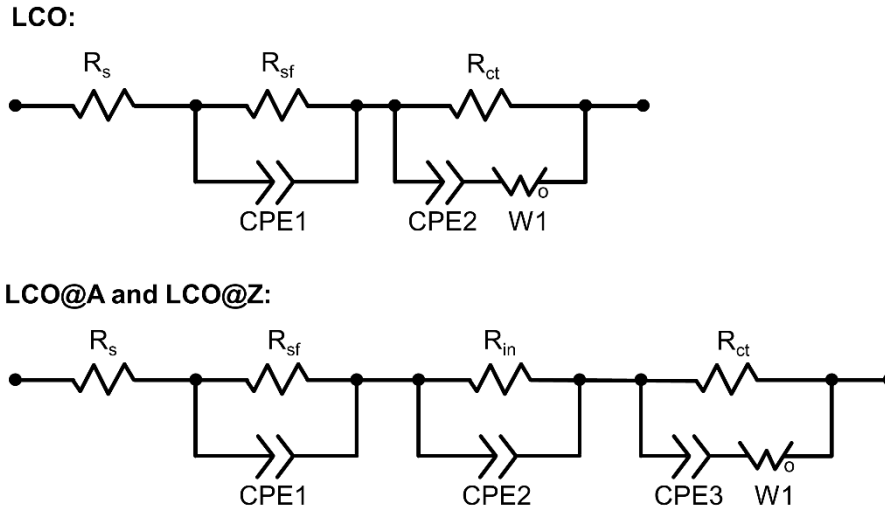
LCO@A and LCO@Z:

Fig. S22 An equivalent electrical circuit that describes the impedance behavior of LCO, LCO@A, and LCO@Z electrodes.
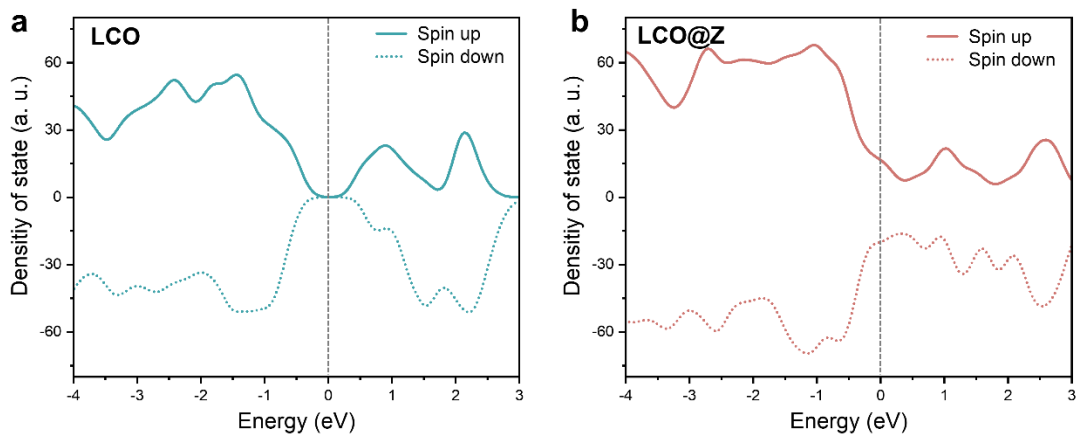
Fig. S23 The calculated density of states (DOS) for LCO and LCO@Z. The Fermi level was set as zero. DOS contributed from spin-up and spin-down channels are distinguished by curves above and below the central axis.
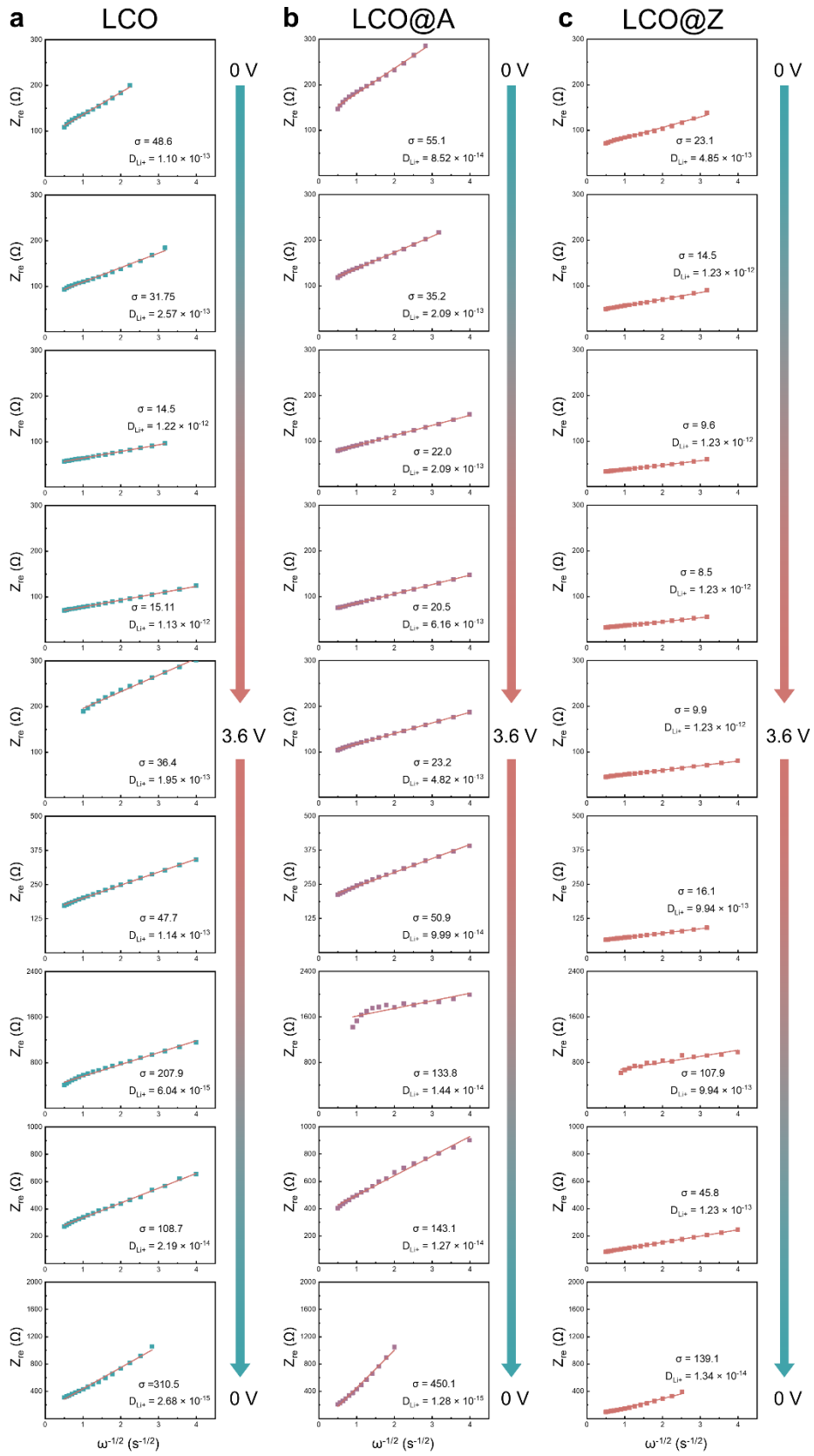
Fig. S24 Plots of the real parts of the complex impedance versus $\omega^{-1/2}$ for **a** LCO, **b** LCO@A, and **c** LCO@Z.
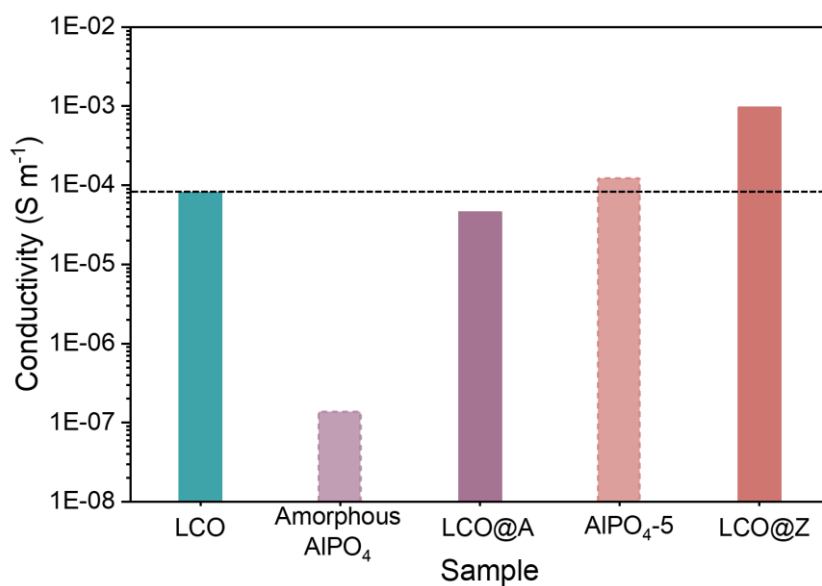
Fig. S25 Electronic conductivities of LCO, amorphous AlPO4, LCO@A, AlPO4-5 and LCO@Z under 10 MPa pressure.
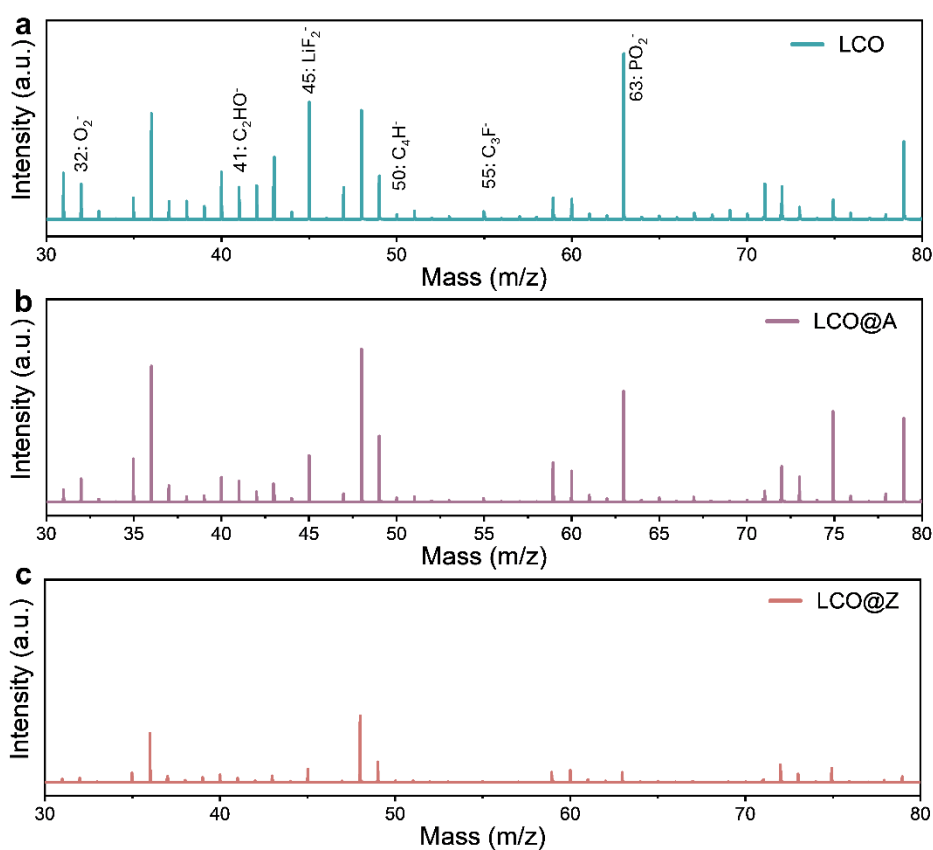
Fig. S26 TOF-SIMS patterns for negative secondary ion mode.
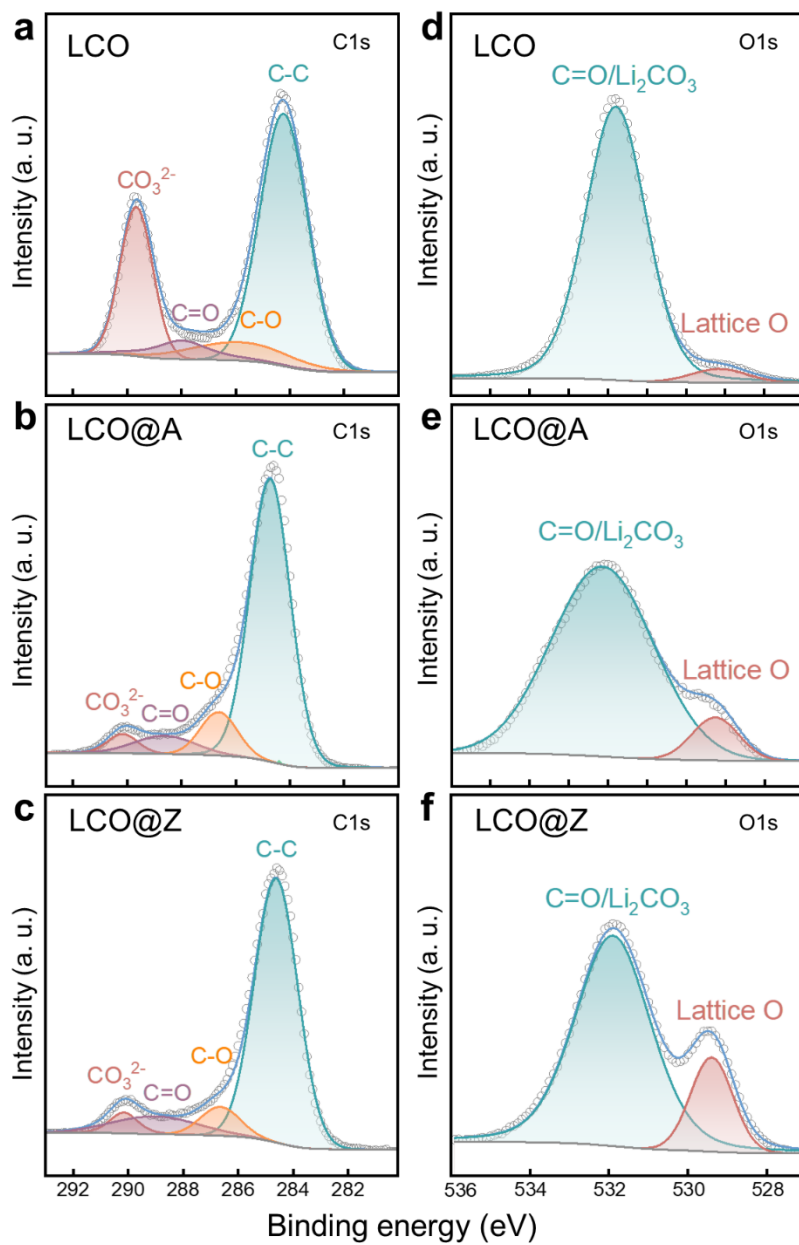
Fig. S27 The **a-c** C1s and **d-f** O1s XPS spectra of LCO, LCO@A and LCO@Z cathode after 200 cycles.
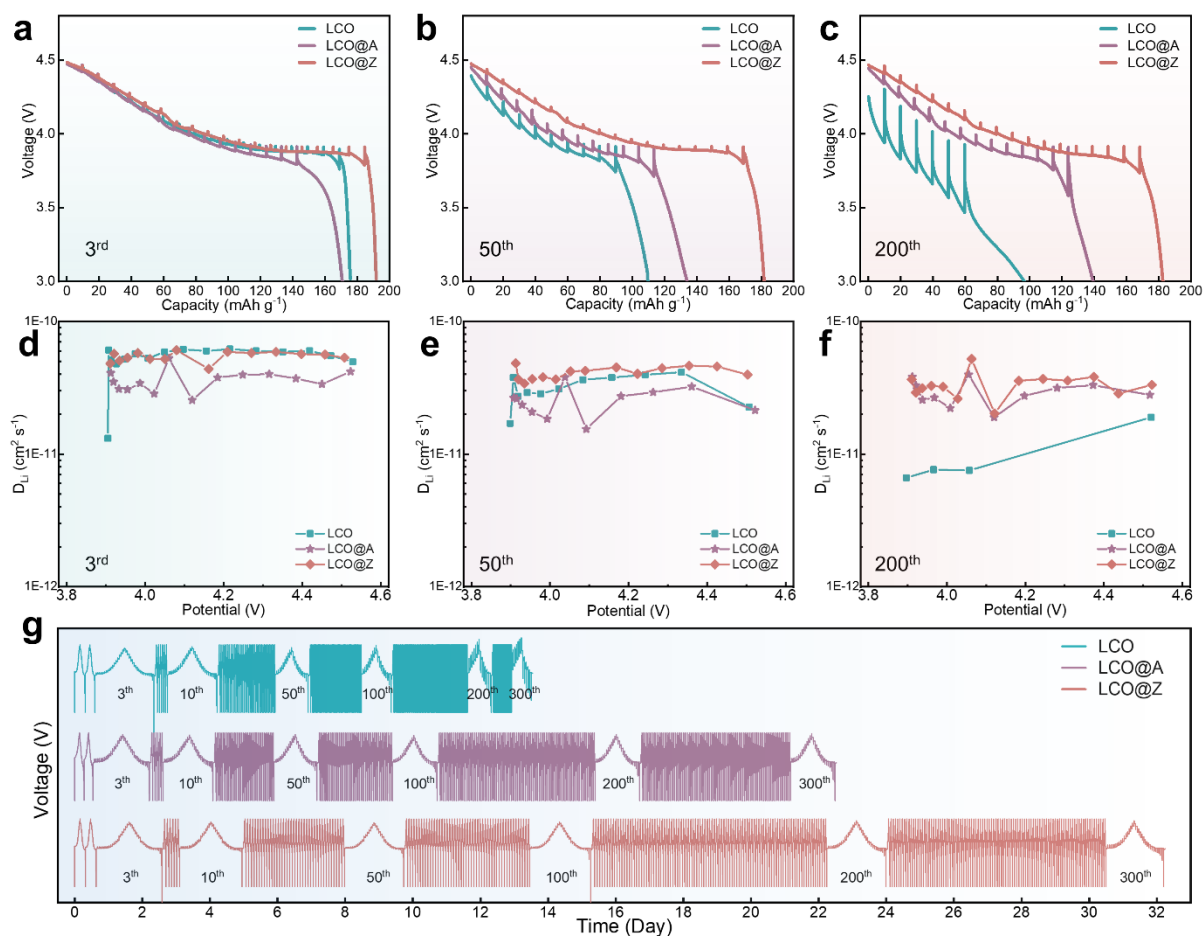
Fig. S28 GITT curves of **a** LCO, **b** LCO@A and **c** LCO@Z at the 3rd, 50th, and 200th cycle. The corresponding Li$^+$ ion diffusion coefficients of **d** LCO, **e** LCO@A and **f** LCO@Z at the 3rd, 50th, and 200th cycle. **g** Cycling performance and overpotential properties of LCO, LCO@A and LCO@Z. GITT measurements are conducted at 0.3 C in the initial two cycles and 1C in the following cycles.

As depicted in **Fig. S28a-c**, LCO@A and LCO@Z demonstrate the smallest electrode polarization from the 3rd to the 200th cycle, whereas LCO exhibits a rapid increase in electrode polarization starting from the 50th cycle. Furthermore, as shown in **Fig. S28g**, LCO@Z requires 32 days to complete 300 cycles, which is longer than LCO (13 days) and LCO@A (22 days). The extended cycling time signifies that LCO@Z exhibits superior cycling stability. The typical potential versus time profiles of LCO, LCO@A, and LCO@Z are illustrated in

Fig. S29, providing further insight into their electrochemical behavior. The evolution of Li$^+$ diffusion coefficient (D_{Li+}) of cathodes during cycling is depicted in **Fig. S28d-f**. During the 3rd cycle, the calculated D_{Li+} values are similar for all the three cathodes. However, as cycling progresses from the 50th to the 200th cycle, the average D_{Li+} of LCO@Z remains almost unchanged, while that of LCO experiences a significant decrease. The GITT results confirm that the effective zeolite coating strategy enhances the Li$^+$ diffusion kinetics of LCO@Z, leading to larger and more stable Li$^+$ diffusion coefficients compared to LCO and LCO@A. A linear relationship between potential and $\tau^{1/2}$ can be observed, and D_{Li+} can be calculated based on the equation (1)

$$D = \frac{4}{\pi\tau}\left(\frac{mV_M}{MA}\right)^2\left(\frac{\Delta E_S}{\Delta E_\tau}\right)^2 \tag{1}$$

where m and M indicate the mass and molar mass of the electrode material, respectively. V_M (cm^3 mol^{-1}) refers to their molar volume, and A (cm^2) stands for their active area.
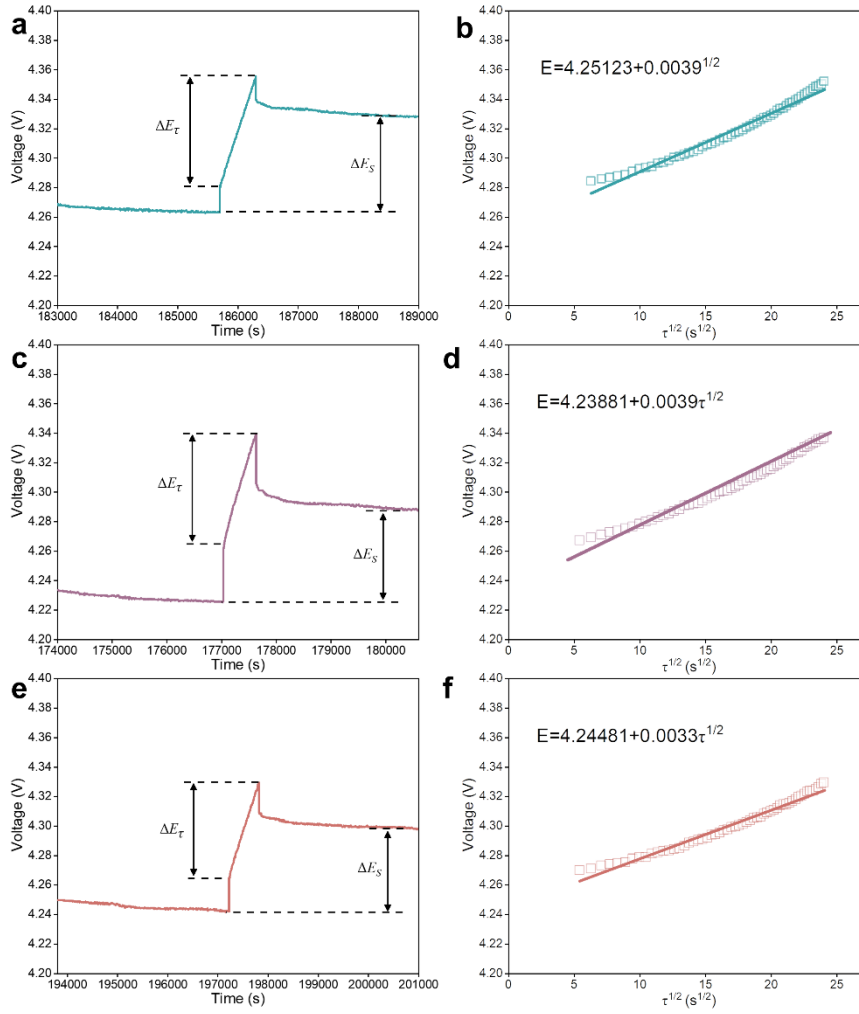
Fig. S29 A typical voltage versus time profile of **a** LCO, **c** LCO@A and **e** LCO@Z. A linear relationship between voltage and $\tau^{1/2}$ of **b** LCO, **d** LCO@A and **f** LCO@Z.
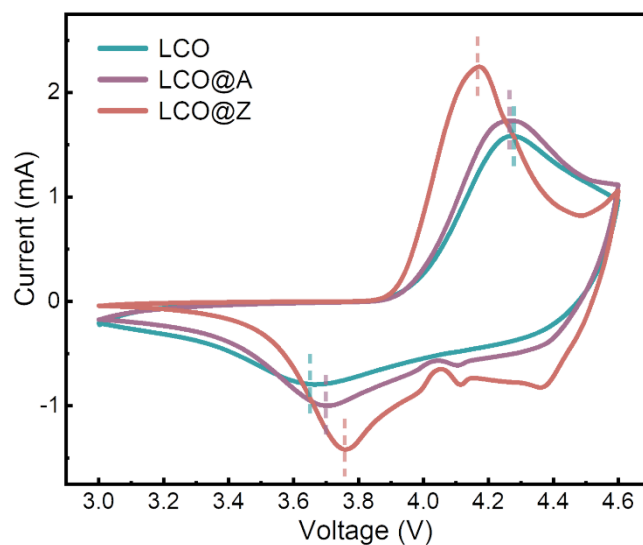
Fig. S30 Cyclic voltammetry of bare LCO, LCO@A and LCO@Z after 200 cycles.

The redox behaviors of the cathodes are investigated through cyclic voltammetry (CV), as shown in **Fig. S30**. After 200 cycles, the redox peaks of LCO@Z remain sharp, indicating higher reversibility of the redox reactions in the LCO@Z cathode. This observation suggests a significant improvement in cycling stability following surface engineering. On the other hand, the redox peaks of LCO decrease, confirming the occurrence of irreversible structural evolutions after high-voltage long-term cycling.

Table S1 Quantitative analysis of the Al, P in LCO@Z-0.5% powder by ICP-OES.

Sample		Elemental content (g kg^{-1})	Molar ratio of Al/Co or P/Co
LCO@Z-0.5%	Co	619.11	/
	Li	95.11	/
	Al	1.14	0.41%
	P	1.21	0.37%

Table S2 Performance comparison of capacity retention of various surface-modified commercial LCO cathodes under high voltage.

Modification strategy	Rate	Retention (%)	Journal
$AlPO_4$-5 zeolite coated $LiCoO_2$ (LCO@Z)	1C	94.6% after 100 cycles 90.3% after 200 cycles	This work
[1] LCO@Carbonate	1C	90.9% after 100 cycles	Advanced Materials (2024)[7]
[2] LCO@RbAlF$_4$	0.3C	90.2% after 100 cycles	Advanced Science (2022)[8]
[3] LCO@MXenes	0.5C	86.2% after 100 cycles	Advanced Functional Materials (2023)[9]
[4] LCO@Lu	0.5C	86.2% after 150 cycles	Advanced Functional Materials (2022)[10]
[5] LCO@LiCoPO$_4$	1C (30℃)	92.0% after 200 cycles	Advanced Energy Materials (2022)[11]
[6] LCO@Li$_3$NbO$_4$	0.2C	90.9% after 200cycles	Advanced Materials (2023)[12]
[7] LCO@LiFe$_{0.4}$Mn$_{0.6}$PO$_4$	1C	85.4% after 200 cycles	Advanced Functional Materials (2023)[13]
[8] LCO@Al-F	0.5C	86.9% after 200cycles	Advanced Energy Materials (2022)[14]
[9] LCO@Li-Al-F	0.5C	82.6% after 200 cycles	Advanced Functional Materials (2022)[15]
[10] LCO@Li/Al/F	0.1C	81.8% after 200 cycles	Nature Communications (2018)[16]
[11] LCO@Li$_2$CoTi$_3$O$_8$	0.1C	81.2% after 200 cycles	Advanced Science (2022)[17]
[12] LCO@Rock-Salt	1C (4.65V)	85.9% after 300 cycles	Advanced Energy Materials (2024)[18]
[13] LCO@Nanofilm	1C (4.7V)	85.7% after 300 cycles	Angewandte Chemie International Edition (2024)[19]
[14] LCO@polyanionic	1C	84% after 300 cycles	Energy & Environmental Science (2024)[20]

Table S3 The simulated results from EIS spectra of LCO, LCO@A, and LCO@Z at various state of charges (SOCs) during the second charge/discharge cycle.

Samples	SOC	Simulated electrochemical parameters				
		$R_{sf}(\Omega)$	$R_{in}(\Omega)$	$R_{ct}(\Omega)$	$\sigma\,(\Omega \cdot cm^2\,mol^{-1})$	$D_{Li+}(cm^2 \cdot s^{-1})$
LCO	Charged to 4.0 V	17.1	/	81.7	48.6	1.10×10^{-13}
	Charged to 4.15 V	17.3	/	73.8	31.7	2.57×10^{-13}
	Charged to 4.3 V	25.9	/	26.2	14.5	1.22×10^{-12}
	Charged to 4.45 V	29.6	/	37.3	15.11	1.13×10^{-12}
	Charged to 4.6 V	35.4	/	179.9	36.4	1.95×10^{-13}
	Discharged to 4.45 V	73.1	/	101.8	47.7	1.14×10^{-13}
	Discharged to 4.3 V	127.9	/	80.5	207.9	6.04×10^{-15}
	Discharged to 4.15 V	132.5	/	88.9	108.7	2.19×10^{-14}
	Discharged to 4.0 V	99.89	/	155.2	310.5	2.68×10^{-15}
LCO@A	Charged to 4.0 V	15.2	27.4	134.9	55.1	8.52×10^{-14}
	Charged to 4.15 V	19.1	22.3	199.8	35.2	2.09×10^{-13}
	Charged to 4.3 V	22.8	14.4	36.3	22.0	5.34×10^{-13}
	Charged to 4.45 V	24.3	13.8	36.1	20.5	6.16×10^{-13}
	Charged to 4.6 V	28.2	12.1	72.5	23.2	4.82×10^{-13}
	Discharged to 4.45 V	92.9	40.2	104.9	50.9	9.99×10^{-14}
	Discharged to 4.3 V	79.7	85.5	140.3	133.8	1.44×10^{-14}
	Discharged to 4.15 V	95.3	97.3	180.5	143.1	1.27×10^{-14}
	Discharged to 4.0 V	100.2	99.6	219.9	450.1	1.28×10^{-15}
LCO@Z	Charged to 4.0 V	12.1	21.9	50.2	23.1	4.83×10^{-13}
	Charged to 4.15 V	9.3	15.4	29.3	14.5	1.23×10^{-12}
	Charged to 4.3 V	7.5	6.1	21.4	9.6	2.81×10^{-12}
	Charged to 4.45 V	8.5	5.3	18.9	8.5	3.58×10^{-12}
	Charged to 4.6 V	11.3	9.5	24.3	9.9	2.65×10^{-12}
	Discharged to 4.45 V	11.5	9.5	25.1	16.1	9.94×10^{-13}
	Discharged to 4.3 V	7.1	6.4	15.1	107.9	2.22×10^{-14}
	Discharged to 4.15 V	12.2	27.9	34.3	45.8	1.23×10^{-13}
	Discharged to 4.0 V	12.9	29.2	43.8	139.1	1.34×10^{-14}

Table S4 Electronic conductivities of LCO, amorphous AlPO$_4$, LCO@A, AlPO$_4$-5 and LCO@Z under 10 MPa pressure.

Sample	LCO	Amorphous AlPO$_4$	LCO@A	AlPO$_4$-5	LCO@Z
Conductivity (S m^{-1})	8.07×10^{-5}	1.34×10^{-7}	4.56×10^{-5}	1.21×10^{-4}	9.59×10^{-4}

Table S5 Quantitative analysis of the Co and Li contents in cycled Li metal anodes paired with LCO, LCO@A and LCO@Z cathodes by ICP-OES.

Sample		LCO	LCO@A	LCO@Z
Quality (ug kg^{-1})	Co	12264	5109	665
	Li	2.25×10^7	2.40×10^7	2.18×10^7
Molar ratio (Co/Li)		4.736 ‰	1.793 ‰	0.249 ‰

Reference

1. G. Kresse and J. Furthmüller, *Phys. Rev. B*, 1996, **54**, 11169.

2. G. Kresse and D. Joubert, *Phys. Rev. B*, 1999, **59**, 1758.

3. J. P. Perdew, K. Burke and M. Ernzerhof, *Phys. Rev. Lett.*, 1996, **77**, 3865.

4. S. Grimme, J. Antony, S. Ehrlich and H. Krieg, *J. Chem. Phys.*, 2010, **132**, 154104.

5. A. Jain, S. P. Ong, G. Hautier, W. Chen, W. D. Richards, S. Dacek, S. Cholia, D. Gunter, D. Skinner, G. Ceder and K. A. Persson, *APL Mater.*, 2013, **1**, 011002.

6. G. Henkelman, B. P. Uberuaga and H. Jónsson, *J. Chem. Phys.*, 2000, **113**, 9901-9904.

7. H. Liao, M. Cai, W. Ma, Y. Cao, S. Zhao, Y. Dong and F. Huang, *Adv. Mater.*, 2024, **n/a**, e2402739.

8. T. Fan, Y. Wang, V. K. Harika, A. Nimkar, K. Wang, X. Liu, M. Wang, L. Xu, Y. Elias, H. Sclar, M. S. Chae, Y. Min, Y. Lu, N. Shpigel and D. Aurbach, *Adv. Sci.*, 2022, **9**, e2202627.

9. C. Sun, B. Zhao, J. Mao, K. H. Dai, Z. y. Wang, L. b. Tang, H. z. Chen, X. h. Zhang and J. c. Zheng, *Adv. Funct. Mater.*, 2023, **33**, 2300589.

10. J. Xia, N. Zhang, Y. Yang, X. Chen, X. Wang, F. Pan and J. Yao, *Adv. Funct. Mater.*, 2022, **33**, 2212869.

11. X. R. Yang, C. W. Wang, P. F. Yan, T. P. Jiao, J. L. Hao, Y. Y. Jiang, F. C. Ren, W. G. Zhang, J. M. Zheng, Y. Cheng, X. S. Wang, W. Yang, J. P. Zhu, S. Y. Pan, M. Lin, L. Y. Zeng, Z. L. Gong, J. T. Li and Y. Yang, *Adv. Energy Mater.*, 2022, **12**, 2200197.

12. Y. Yan, Q. Fang, X. Kuai, S. Zhou, J. Chen, H. Zhang, X. Wu, G. Zeng, Z. Wu, B. Zhang, Y. Tang, Q. Zheng, H. G. Liao, K. Dong, I. Manke, X. Wang, Y. Qiao and S. G. Sun, *Adv. Mater.*, 2024, **36**, e2308656.

13. Y. Yan, S. Zhou, Y. Zheng, H. Zhang, J. Chen, G. Zeng, B. Zhang, Y. Tang, Q. Zheng, C. Wang, C. W. Wang, H. G. Liao, I. Manke, X. Kuai, K. Dong, Y. Sun, Y. Qiao and S. G. Sun, *Adv. Funct. Mater.*, 2023, **34**, 2310799.

14. W. Huang, Q. Zhao, M. Zhang, S. Xu, H. Xue, C. Zhu, J. Fang, W. Zhao, G. Ren, R. Qin, Q. Zhao, H. Chen and F. Pan, *Adv. Energy Mater.*, 2022, **12**, 2200813.

15. T. Fan, W. Kai, V. K. Harika, C. Liu, A. Nimkar, N. Leifer, S. Maiti, J. Grinblat, M. N.

Tsubery, X. Liu, M. Wang, L. Xu, Y. Lu, Y. Min, N. Shpigel and D. Aurbach, *Adv. Funct. Mater.*, 2022, **32**, 2204972.

16. J. Qian, L. Liu, J. Yang, S. Li, X. Wang, H. L. Zhuang and Y. Lu, *Nat. Commun.*, 2018, **9**, 4918.

17. S. Mao, Z. Shen, W. Zhang, Q. Wu, Z. Wang and Y. Lu, *Adv. Sci.*, 2022, **9**, e2104841.

18. W. Ding, H. Ren, Z. Li, M. Shang, Y. Song, W. Zhao, L. Chang, T. Pang, S. Xu, H. Yi, L. Zhou, H. Lin, Q. Zhao and F. Pan, *Adv. Energy Mater.*, 2024, **14**, 2303926.

19. J. Yao, Y. Li, T. Xiong, Y. Fan, L. Zhao, X. Cheng, Y. Tian, L. Li, Y. Li, W. Zhang, P. Yu, P. Guo, Z. Yang, J. Peng, L. Xue, J. Wang, Z. Li, M. Xie, H. Liu and S. Dou, *Angew. Chem., Int. Ed.*, 2024, **63**, e202407898.

20. W. Zheng, G. Liang, H. Guo, J. Li, J. Zou, J. A. Yuwono, H. Shu, S. Zhang, V. K. Peterson, B. Johannessen, L. Thomsen, W. Hu and Z. Guo, *Energy Environ. Sci.*, 2024, **17**, 4147-4156.